Journal of Colloid and Interface Science 633 (2023) 526–535

Contents lists available at ScienceDirect

Journal of Colloid and Interface Science

journal homepage: www.elsevier.com/locate/jcis

Membrane permeability based on mesh analysis

Björn Stenqvist [a,*], Marica B. Ericson [b], Sebastien Gregoire [c], Bruno Biatry [c], Guillaume Cassin [c], Marija Jankunec [d,e,f], Johan Engblom [d,e], Emma Sparr [a]

[a] Division of Physical Chemistry, Department of Chemistry, Lund University, POB 124, SE-221 00 Lund, Sweden
[b] Biomedical Photonics Group, Department of Chemistry and Molecular Biology, University of Gothenburg, SE-412 96 Gothenburg, Sweden
[c] L'Oreal Research & Innovation, 1, avenue Eugène Schueller, 93601 Aulnay-sous-Bois, France
[d] Department of Biomedical Science, Faculty of Health and Society, Malmö University, SE-205 06 Malmö, Sweden
[e] Biofilms - Research Center for Biointerfaces, MalmöUniversity, SE-20506 Malmö, Sweden
[f] Institute of Biochemistry Life Sciences Center, Vilnius University, LT-10257 Vilnius, Lithuania

GRAPHICAL ABSTRACT

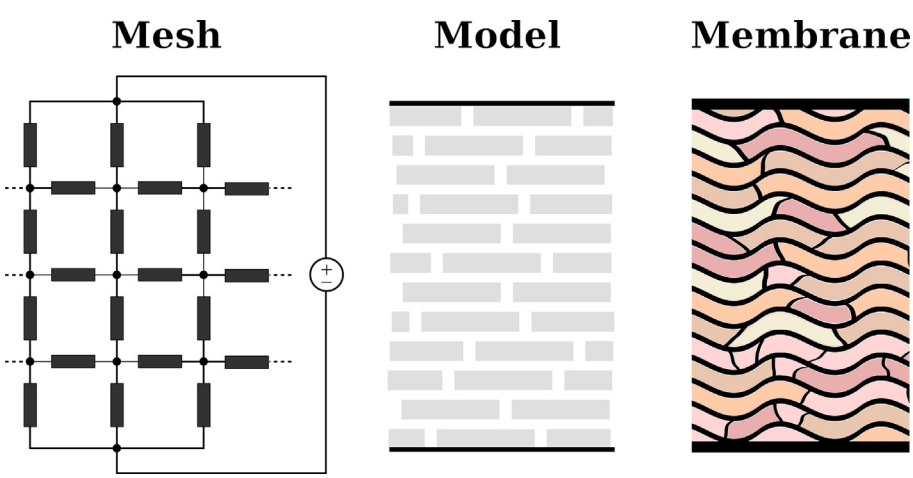

ARTICLE INFO

Article history:
Received 8 August 2022
Revised 11 October 2022
Accepted 4 November 2022
Available online 14 November 2022

Keywords:
Membrane
Stratum corneum
Tortuosity
Fick's law
Brick and mortar

ABSTRACT

The main function of a membrane is to control the exchange of matter between the surrounding regions. As such, accurate modeling of membranes is important to properly describe their properties. In many cases in both biological systems and technical applications, the membranes are composite structures where transport properties may vary between the different sub-regions of the membrane. In this work we develop a method based on Mesh analysis that is asymptotically exact and can describe diffusion in composite membrane structures. We do this by first reformulating a generalized Fick's law to include the effects from activity coefficient, diffusion coefficient, and solubility using a single condensed parameter. We then use the derived theory and Mesh analysis to, in essence, retrieve a finite element method approach. The calculated examples are based on a membrane structure that reassembles that of the brick and mortar structure of stratum corneum, the upper layer of our skin. Resulting concentration profiles from this procedure are then compared to experimental results for the distribution of different probes within intact stratum corneum, showing good agreement. Based on the derived approach we further investigate the impact from a gradient in the fluidity of the stratum corneum mortar lipids across the membrane, and find that it is substantial. We also show that anisotropic organisation of the lipid mortar

* Corresponding author.
E-mail address: bjorn.stenqvist@teokem.lu.se (B. Stenqvist).

https://doi.org/10.1016/j.jcis.2022.11.013
0021-9797/© 2022 The Authors. Published by Elsevier Inc.
This is an open access article under the CC BY license (http://creativecommons.org/licenses/by/4.0/).

can have large impact on the effective permeability compared to isotropic mortar lipids. Finally, we examine the effects of corneocyte swelling, and their lateral arrangement in the membrane on the overall membrane permeability.

© 2022 The Authors. Published by Elsevier Inc. This is an open access article under the CC BY license (http://creativecommons.org/licenses/by/4.0/).

The main function of membranes found in both biological systems and technical applications is to control the exchange of matter between the surrounding regions. Here, the precise membrane barrier properties are essential to the membrane barrier function. In many cases, the membrane itself has a more or less complex composition and structure. Examples of this include the brick and mortar arrangements relevant for the upper layer of the skin, porous granular material present in sand, and channels modeling percolation of water in soil, all depicted in Fig. 1. The membrane barrier function is then determined by its internal structure, as well as the solubility and the mobility of the diffusing compound in the different membrane regions.

The human skin is one important example of a barrier membrane that separate two profoundly different regions, that is the water-rich inside of our body, and the outside environment that is often dry and may vary substantially during a normal day. As such, the skin protects us from uncontrolled water loss, and it also prevents from uptake of harmful chemicals. The barrier function of the skin is mainly assured by its outermost thin layer, stratum corneum (SC), which consists of dead keratin filled cells (corneocytes) embedded in a lipid matrix in a brick and mortar-like arrangement [1]. The extracellular lipid mortar has a multilamellar structure with an average orientation of the lamelleas parallel to the skin surface[2], implying anisotropy in its diffusion properties. In a realistic description, one need to consider that there are several gradients across SC, which may also lead to variations in the lipid and corneocyte structures at varying depths in the membrane [3,4]. Taken together, the structural complexity of stratum corneum involve both the brick and mortar arrangement, as well as mortar anisotropy and variations in self-assembly structure at varying depths, and these aspects will all impact on the stratum corneum barrier function.

There are several studies in the literature that presents theoretical models for diffusional transport in composite structures, where transport properties may vary between the different subregions of the membrane[5–8]. Those models often treats specific geometries as well as molecules that favor a specific route through the composite structure, for example only go through the mortar in a brick and mortar structured membrane. Many models take into account the brick and mortar structure of SC to model skin permeability[9] with more or less complex geometrical description of corneocyte shape[10]. None of them, however, investigated lipid anisotropy or gradients in fluidity of lipid domain. In this work, the main goal is to formulate a model that accounts for the different molecular aspects of diffusion and partitioning in any type of heterogenous anisotropic composite membrane (see Fig. 1 for examples), allowing for different transport routes. In addition, we include aspects of anisotropic diffusion and gradients in the properties of the different regions of the composite structure. We do this by formulating steady-state diffusion transport through a model membrane with any internal structure using Mesh analysis. While the model is capable of describing different geometries, we here solely focus on the brick and mortar geometry. Still, all the different geometries of porous composite membranes depicted in Fig. 1 are incorporated in the software code used to perform the calculations in this work[11].

The layout of the work is as follows. First, we derive a representation of Fick's law based on the here introduced entity of *momentum permeability*. That entity combines the activity coefficient, mobility (i.e. $\sim$ diffusion coefficient), and solubility into a single parameter without any loss of generality. Based on the presented formalism we then describe a method founded on Mesh analysis, which among others give fluxes, permeabilities and concentration profiles. We then evaluate the method on a membrane structure relevant to stratum corneum. In relation to SC, the tortuous route corresponds to diffusion of a hydrophobic molecule in a membrane with impermeable corneocytes. The present analysis consider both cases of impermeable and permeable bricks, thus accounting for diffusion of both hydrophobic, hydrophilic and intermediate polarity molecules in the SC brick and mortar structure. It is thus an extension of a previous study that only treat the case of turtous diffusional transport of molecules that are not soluble in the bricks [8]. In order to validate the relevance of the present model, the calculated concentration profiles are compared with experimental data on the distribution of model compounds in porcine stratum corneum, as measured by multiphoton laser scanning microscopy. The model compounds include one hydrophobic molecule, rhodamine B hexyl ester (RBHE), and one more hydrophilic molecule,

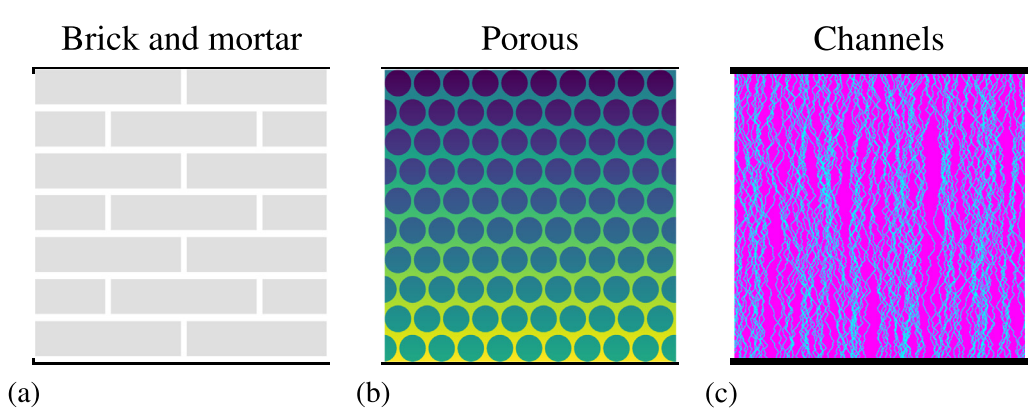

Fig. 1. Three different examples of membrane architectures with composite structures. In this work we treat the situation where the chemical potential of the diffusing substance is constant at the horizontal interfaces (straight lines). Apart from this condition, the model allows for any internal geometric structure and any properties of the building blocks in terms of activity coefficients, diffusion coefficients, and/or solubility of the diffusing compound.

sulphorhodamine B (SRB). Finally, based on the Mesh analysis method we investigate the impact from introducing a gradient in lipid self-assembly structure, anisotropy of the extracellular lipid matrix, corneocyte swelling, as well as changing the lateral arrangement of the corneocytes.

1. Theory

In this section we start by introducing the basic theory of mass transport which the work will be based upon. We then generalize the theory by including the possibility for non-ideal systems with variations in the local solubility of the diffusing molecules. After this, we in detail outline the Mesh analysis approach and how it is used in order to describe transport through a heterogeneous membrane with composite structure. Lastly, we compare the results obtained with the Mesh analysis with analytic theory for the two extreme limit scenarios.

1.1. Mass transport

Ideal steady-state diffusion is commonly described by Fick's first law which is based on the concentration gradient in the system[12]

$$j = -D\nabla c. \tag{1}$$

Here j [kg/m^{2}s] is the flux, D [m^2/s] the diffusion coefficient, and c [kg/m^3] the concentration. For non-ideal systems, however, Eq. 1 does not apply and one need to use a generalised form based on the gradient in chemical potential[13,14]

$$j = -Uc\nabla\mu, \tag{2}$$

where U [m/s/N] is the mobility (drift velocity per unit force), and μ [J] the chemical potential. For the next step we need the standard concentration c° [kg/m^3], which is constant[15], the activity coefficient γ [unitless], and the standard absolute activity $\lambda^\circ = \exp(\mu^\circ/k_BT)$ [unitless], where the standard chemical potential μ° [J] relates to the solubility of the diffusing compound in the medium, k_B [J/K] is the Boltzmann constant, and T [K] the temperature. By combining these into a single measure of solubility and the (inverse) activity coefficient $S = c^\circ/\gamma\lambda^\circ$ [kg/m^3], and note that if

$$\frac{\partial S}{\partial c} = 0, \tag{3}$$

i.e. the activity and solubility of the diffusing compound does not change with a change in concentration, then we get the simple relationship between the mobility and diffusion coefficient, $D = Uk_BT$. This can be realized if c in Eq. 1 is replaced by $c = \exp((\mu - \mu^\circ)/k_BT)c^\circ/\gamma$ [15] and the equation is then compared to Eq. 2. In the following, Eq. 3 is assumed to hold, and thus $D = Uk_BT$. Similar to λ° we now present the absolute activity $\lambda = \exp(\mu/k_BT)$ [unitless], which is a rewritten form of the chemical potential. Through the definition of activity[15] we then acknowledge that λ relates to the concentration as

$$c = S\lambda. \tag{4}$$

By further exploiting the relationship between λ and μ Eq. 2 can be rewritten as

$$j = -\chi\nabla\lambda \tag{5}$$

where we have introduced the *momentum permeability* $\chi = Uk_BTS$ = [assuming Eq. 3] $= DS$ [kg/ms]. With this definition, we condense the activity coefficient, mobility ($\sim$ diffusion coefficient), and solubility into a single efficient diffusion parameter, χ, without losing any generality. Just as the diffusion coefficient D is a measure of the velocity of a diffusing compound, χ is a measure of its momentum (i.e. mass $\times$ velocity). In the present context, χ is thus a product between how much substance that is soluble (S) and how fast it diffuse ($\sim D$). Finally we present the definition of permeability P [m/s] as [12]

$$P = -\frac{j}{\Delta c}, \tag{6}$$

where the flux j through that membrane relates to the difference in concentration Δc over the same. This entity will be used below to analyse the results from the Mesh analysis.

1.2. Mesh analysis

In this section we present an approach based on Mesh analysis that will be used to retrieve the absolute activity, λ, throughout a discretized model membrane.[16] As we have seen in the previous section, the absolute activity can then be used to retrieve concentration profiles (Eq. 4), fluxes (Eq. 5) and permeabilities (Eq. 6). A similar scheme has been used for studies of a stratum corneum model membrane [6], yet the here presented approach is in many aspects different and more general in its applicability.

In analogy with electric theory we in Fig. 2a present a circuit diagram of a laterally periodic setup (dotted lines) consisting of vertical and horizontal resistors (dark grey blocks), which are linked through nodes (black dots) and connected to an external potential difference. Note that though we here use a 2D laterally periodic system, the mesh in Fig. 2a can be customized to yield a variety of structures including 3D non-periodic systems. The procedure is thus not limited to the here presented geometry, but can be adapted to describe also other structures. The differences between different boundary conditions lie in the composition of the matrix $\mathbf{R}$, which is introduced below. As indicated in Fig. 2b the Mesh setup can, for instance, be used to model a brick and mortar membrane (Fig. 2c) by choosing resistances in the grid that compares to the properties at the corresponding coordinate of the brick and mortar structure. The entities analogous to the electric potential and resistance using Fick's law (Eq. 5) instead of Ohm's law for diffusion of charge is the absolute activity difference $\Delta\lambda$ between start- and end-points for the diffusion, and chemical resistance R [s/kg] defined as

$$R \equiv \frac{\Delta\lambda}{\dot{m}}. \tag{7}$$

In Eq. 7 the mass flow $\dot{m} = -jA$ [kg/s] is the direct analogue of electric current through the area A [m^2]. This further entails that the resistance is inversely proportional to the momentum permeability, or

$$R = \frac{1}{\chi A}. \tag{8}$$

The principle of Mesh analysis is founded on conservation of some entity, here mass, and by utilizing this restriction in every node of a mesh we get

$$\frac{\lambda - \lambda^l}{R^l} + \frac{\lambda - \lambda^r}{R^r} + \frac{\lambda - \lambda^a}{R^a} + \frac{\lambda - \lambda^b}{R^b} = 0. \tag{9}$$

Here λ is the absolute activity in that node, and the superscript $\{l, r, a, b\}$ index the component just {left,right,above,below} of that node in the mesh. By applying Eq. 9 to every node, i.e. mass conservation everywhere, together with a known mesh of resistors (or χ) and a known absolute activity difference over the entire membrane, we can arrange all of the given equations into a single matrix equation

$$\mathbf{R}^{-1}\boldsymbol{\lambda} = \dot{\mathbf{m}}, \tag{10}$$

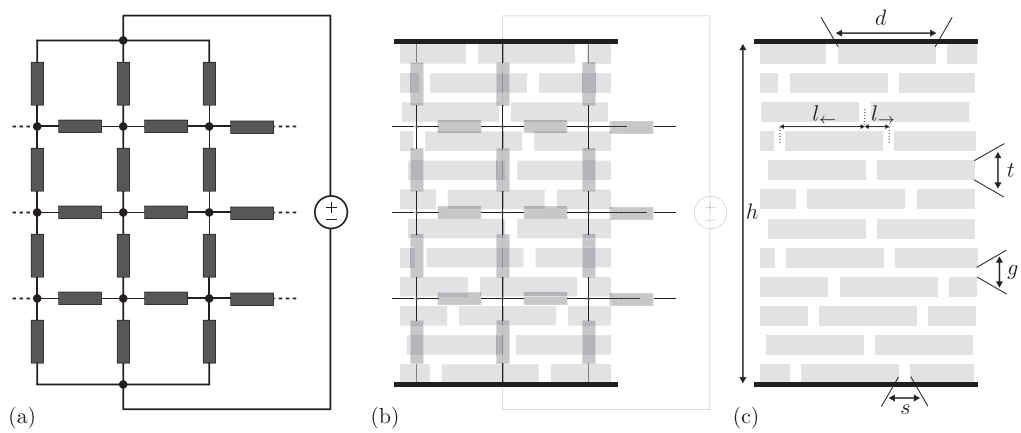

Fig. 2. (a) Circuit diagram of resistors modelling a membrane, e.g. a brick and mortar system (c). Dashed lines implies periodic boundaries which continue into the dotted lines on the opposing side of the diagram. In (b) we present a combined figure of (a) and (c) that show which resistor that corresponds to which part in the model. Essential geometric parameters are presented in (c).

c.f. Eq. 5. For a $N \times M$ mesh of nodes as in Fig. 2a (excluding the single top and single bottom nodes), the dimension of $\mathbf{R}^{-1}$ is $NM \times NM$, and the dimension of $\boldsymbol{\lambda}$ and $\dot{\mathbf{m}}$ are both $NM \times 1$. We now denote Λ_a/Λ_b as absolute activity above/below the top/bottom resistors. In Eq. 10 $\dot{\mathbf{m}}$ consists of mass flow elements of the form Λ_a/R^v_{1m} and Λ_b/R^v_{Nm}, where the double index denotes the row and column of the resistors of the mesh, and v that the resistor is vertical. $\boldsymbol{\lambda}$ is a single column matrix including every node absolute activity and this is what we aim to retrieve. By calculating the inverse of $\mathbf{R}^{-1}$ we get

$$\boldsymbol{\lambda} = \mathbf{R}\dot{\mathbf{m}} \tag{11}$$

and now all absolute activities in the nodes are known which can then be used to calculate concentration profiles, fluxes, and permeabilities of the entire mesh.

1.3. Comparing Mesh model to exact asymptotic expressions

In this section we examine the brick and mortar model in two extreme scenarios; when the permeability is infinitely higher in bricks as compared to the mortar, and vice verse. Both these cases have known analytic solutions which can be used in the validation of the mesh analysis approach. We start by investigating the case when bricks have lower resistance to the flux than the mortar, and the resistance to the flux lies only in the mortar. For this case, we use a model where bricks are considered to have an infinite width, which is a fair assumption when the mortar in the lateral spacing in-between bricks can be neglected (Fig. 2c). This gives a model with alternating brick/mortar layers which has an exact analytic solution for the flux[12], and thus also the membrane permeability, which we will come back to later.

For the other extreme case of completely impermeable bricks we need to examine the concept of tortuosity[17,8] and relate it to membrane permeability. By assuming impermeable bricks, the tortuosity τ [unitless] of that system based on Eq. 5 and Eq. 7 is

$$\tau = 1 + \frac{d}{s} + (N-1) \cdot \frac{L^2}{gh} \frac{\omega}{(1+\omega)^2}. \tag{12}$$

following the same procedure as previously described in [8]. In Eq. 12 (and Fig. 2c) d [m] is the brick width, s [m] the lateral spacing between bricks, N [unitless] the number of layers of bricks, L [m] is the period of the system, g [m] the vertical spacing between bricks, $h = Nt + (N-1)g$ [m] the total thickness of the membrane where t [m] is the thickness of the bricks, and ω [unitless] the offset ratio. The latter is a measure of the lateral arrangement of the bricks and for the extreme case $\omega = 1$, corresponding to the case illustrated in Fig. 1a, there is a maximal tortuous path for molecules diffusing exclusively in the mortar. For the case of $\omega = 0$ (or equivalently $\omega = \infty$), the bricks are arranged in perfect stacks above/beneath one another. In this case there is a straight path between the bricks solely in the mortar from the top to the bottom of the membrane. The tortuosity is defined[18] as $\tau = j_0/j_N$, where j_0 is the flux through a reference membrane consisting of only mortar (i.e. no bricks), and j_N is the flux through an equally thick model membrane with N layers of bricks. As the flux through a uniform reference membrane j_0 is trivial to calculate analytically by using Eq. 5 we then get $j_N = j_0/\tau$. By finally using Eq. 6 we get the relationships

$$\tau = \frac{j_0}{j_N} = \frac{P_0}{P_N}. \tag{13}$$

The inverse tortuosity can thus also be viewed as a measure of the permeability P_N of a membrane relative to the permeability of the reference membrane consisting of only mortar (P_0). As such we relabel $\tau^{-1} = \widehat{P}$ as the *relative permeability* of a membrane and we have

$$\widehat{P} = \frac{P}{P_{Ref.}} = \frac{j}{j_{Ref.}} \tag{14}$$

where *Ref* refers to the homogeneous reference membrane consisting of only mortar.

2. Materials and Experimental methods

The penetration and partitioning of two different fluorescent probes inside skin samples were studied using multiphoton laser scanning microscopy. The skin samples were prepared from porcine ears obtained from a local abattoir. The fresh ears were stored at −80 °C until skin sample preparation. For the preparation, the ears were thawed, the hair was trimmed and the skin from the inner part of the ear was removed with a TCM 3000 BL dermatome (Nouvag AG, Switzerland) with an approximate thickness of 200 μm.

The sheets of skin were mounted in in vitro PermeGear In-Line Diffusion Cells (IL-7, 9 mm diameter orifice)(PermeGear, Inc. Hellertown, USA) with a donor volume of 1 mL, and a receptor flow rate 1.6 mL/h. All experiments were performed at 32 °C, which is considered to be normal skin temperature according to OECD guid-

lines[19]. After 24 h exposure to the test aqueous solutions with the dyes, the skin samples were gently rinsed with water and excess water was carefully dried off with a tissue. The samples were kept frozen at −20°C until use. For the microscopy analysis, the samples were placed directly on microscope slides and protected with cover slips. The skin was in contact with the cover glass to maintain a mechanically stable surface, and placed on the microscope.

The donor solution used were composed of either 0.005% (w/w) rhodamine B hexyl ester (RBHE) (Molecular Probes, USA) or 0.05% (w/w) sulphorhodamine B (SRB) (Sigma Aldrich, Germany) dissolved in phosphate-buffered saline (PBS) pH 7.4 (130.9 mM NaCl (Merck KGaA, Germany), 5.1 mM $Na_2HPO_4 * 2H_2O$ (Fluka Analytical, Germany) and 1.5 mM KH_2PO_4 (Sigma–Aldrich, Germany). All aqueous solutions were prepared using ultra purified water (18.2 MΩcm; PURELAB UHQ II system; ELGA Labwater, UK). As the concentration of the more hydrophobic compound, RBHE, was ten times lower than that of SRB, both dye solutions could be prepared in pure buffer without any additional co-solvent. As the goal of the present studies is to study the distribution of the dyes in the skin rather than to quantify the amount that penetrates the skin, the concentrations of the probes in the solutions were chosen to optimize the conditions for the imaging, meaning that neither their concentration or the activity in the PBS solutions were adjusted to be the same. The concentration of 0.05% SRB in PBS corresponds to less than 2% of the maximum solubility (32.24 mg/ml, unpublished data), while the concentration of 0.005% RBHE in PBS is judged to be close to the saturation limit.

Multiphoton laser scanning microscopy (MPM) was performed using a Zeiss LSM 710 META NLO microscope (Carl Zeiss, Germany), equipped with a tunable mode-locked femtosecond pulsed Ti:Sapphire laser (Mai Tai, Spectra Physics, Mountain View, USA) operating at 780 nm using an earlier reported procedure.[20] For imaging a water immersion objective lens (20x, NA = 1.0) and excitation of 780 nm was utilized. The fluorescence was recorded in both the green (300–485 nm, autofluorescence) and the red (565–610 nm, RBHE and SRB) using non-descanned spectral channels. Only data from the red channel is presented, corresponding to the signal from the applied fluorophore. The spectral crosstalk of autofluorescence in the red spectral channel given these settings was found negligible, as confirmed previously.[21] The focus was changed by using a step-motor sequentially with a step size of 1 μm from the surface of SC to an approximate depth of 80–150 μm. No significant photobleaching was observed in the experiments under the conditions used to quantify penetration. The measured average power of the excitation light just before the microscope objective was 1 mW. The data presented correspond to the first 25 μm of the z-stack matching SC. Three representative cross sections from each sample are here reported for comparison with the theoretical model.

3. Results and discussion

Below we present a number of examples all relevant for transport through SC. The calculations were done for representative SC geometries unless otherwise stated: brick thickness $t = 1\mu$ m, brick width 20μ m, lateral spacing between bricks $s = 0.1\mu$ m, vertical spacing between bricks $g = 0.1\mu$ m, twenty layers of bricks, and offset ratio $\omega = 1$. We make the assumption that the activity coefficient γ is equal to one, which implies that S is proportional to the solubility of a compound. This is done for conciseness and all presented results are valid also for $\gamma \neq 1$ (as long as S is conserved). In the description of the mortar lipids we need to consider that the extracellular lipid mortar contains domains with different properties, including solid and fluid (oil-like) lipids[22]. The proportion of fluid lipids used in the example calculations is 10 % if not otherwise stated, which is the estimated fraction of fluid SC lipids in intact porcine SC at ambient hydration conditions based on ssNMR measurements [23]. We denote the fraction of fluid lipids as Φ_{fluid} [unitless] and we assume zero solubility in the solid lipid regions[12] (Chap. 10). Then the effective mortar solubility $S_M = S_{lipids}$ is defined as

$$S_{lipids} = S_{oil} \cdot \Phi_{fluid} + S_{solid} \cdot \left(1 - \Phi_{fluid}\right) \approx S_{oil} \cdot \Phi_{fluid} \tag{15}$$

where S_{oil} is the solubility of the added compound in the fluid lipid, which is here compared to a fluid hydrocarbon oil, and S_{solid} is the (zero) solubility in the solid lipids. The mortar/brick distribution coefficient $K_{M/B}$ will thus depend on the partition coefficient between a hydrocarbon oil (here meaning the fluid fraction of the SC mortar lipids), and the water-rich corneocyte bricks, which can be approximated by $K_{oil/water}$. Furthermore, the distribution will depend on the amount and organisation of fluid lipids within the mortar lipid regions. If the conditions changes so that the fraction of fluid SC increases, that will thus also lead to an increase in $K_{M/B}$, even though $K_{oil/water}$ of the given molecule is unchanged. The internal organisation of the solid and fluid lipids in the mortar will further impact the effective diffusion in these regions. The calculated profiles presented in this work all correspond to the case of a continuous route in fluid lipids through the extracellular lipid matrix. The effective diffusion coefficient can then be estimated as $D_M = D_{oil} \cdot \Phi_{fluid} + D_{solid\ lipids} \cdot \left(1 - \Phi_{fluid}\right)$, where D_{oil} is the diffusion coefficient in the fluid lipids and $D_{solid\ lipids}$ is the diffusion coefficient in the solid lipids. Finally, we make the assumption that $D_{solid\ lipids} \approx 0$ and can therefore be neglected compared to D_{oil}.

In order to facilitate the comparisons between different systems and conditions, we throughout this work present relative permeabilities ($\widehat{P}$) that are defined as the permeability for a given system (membrane and diffusing compound) normalised with a reference permeability calculated for the membrane geometries described above with $\Phi_{fluid} = 0.1$, and a diffusing substance with $K_{M/B} = S_M/S_B = 1$, and $D_M = D_B = 1$. We also restrict the examples to cases where the product $S_M \cdot S_B = 1 \left(= 10 \cdot \Phi_{fluid}\right)$. In simple terms this mean that a diffusing compound can either have high solubility in the hydrophilic bricks or the lipid mortar or intermediate solubility in both. Lastly, we note that the calculated values are indicated by symbols in the plots, and the connecting lines are obtained through interpolation by cubic splines.

3.1. Comparison between Experimental results and Model calculations

Fig. 3 summarizes the key results of the model calculations together with the fluorescence microscopy images for two different fluorescent probes penetrating into the stratum corneum. The microscopy images can be interpreted as concentration profiles of the different probes inside the stratum corneum. We used two different probes; SRB that is soluble in both polar and apolar solvents (Fig. 3b), and RBHE that is a hydrophobic molecule (Fig. 3c). In the present analysis, we focus on the qualitative differences in how these dyes distribute within the SC, rather than quantification of the local variations in dye concentration. The experimental data can be compared to the calculated concentration profiles in panels Fig. 3d-f for three model compounds with different oil/water partition coefficients (and thus also different mortar/brick distribution), corresponding to one hydrophilic compound (Fig. 3d), one hydrophobic compound (Fig. 3f), and one compound with intermediate polarity (Fig. 3e). The experimental images each consists of three different cross-sections of the sample. The SRB image Fig. 3b show a fairly uniform lateral distribution and a smooth vertical gradient from high concentration at the top to low concentration at the bottom. It is hard to discern any clear

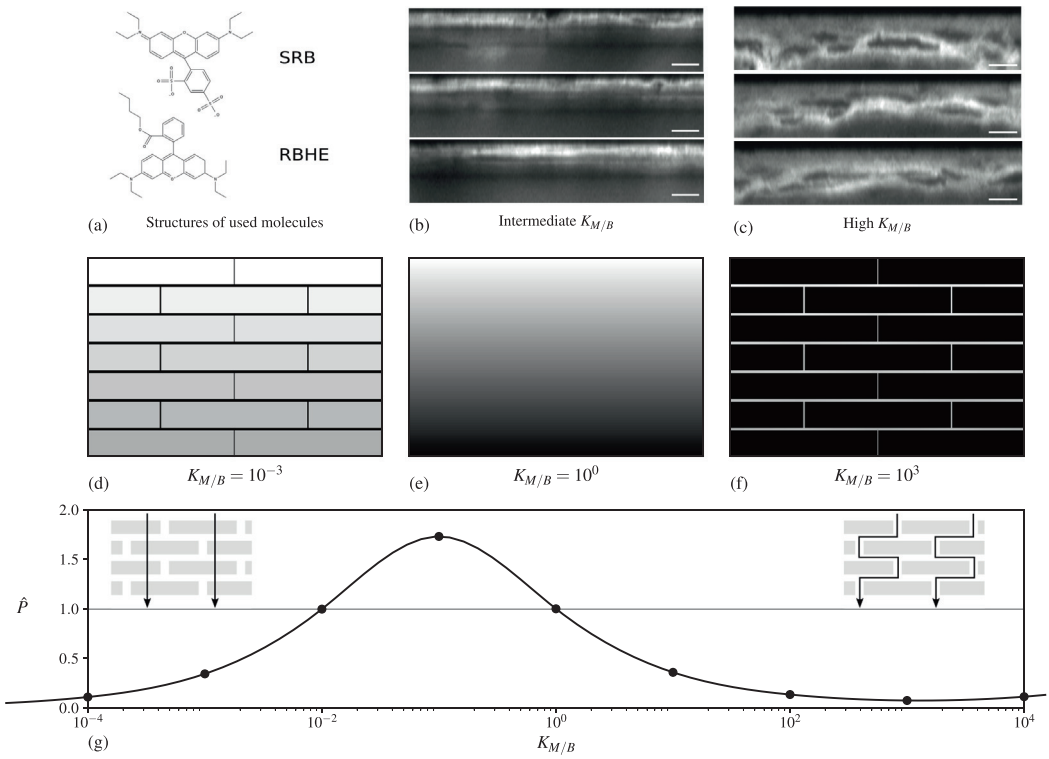

Fig. 3. Molecules used in experiments (a). Multiphoton laser scanning microscopy data for the concentration profiles from stratum corneum samples with the slightly hydrophilic probe SRB (b), and the hydrophobic probe RBHE (c). Scalebar = 10 μm. (d,e,f) Calculated concentration profiles for diffusing molecules with different hydrophobicites, expressed in terms of the the partition coefficient between mortar and bricks. (g) Model calculations of the relative permeability $\widehat{P}$ (see Eq. 14) as a function of the mortar/brick distribution coefficient as compared to a homogeneous reference membrane, i.e.. $K_{M/B} = 1$.

features relating to the underlying structure of the membrane. This is similar to the concentration profiles obtained in the model calculations in Fig. 3e for $K_{M/B} = 10^0$, which also display a gradual monotonic shift from high to low concentration. In contrast, the microscopy image obtained for RBHE (Fig. 3c) show high fluorescence in areas surrounding large regions with low fluorescence which infers a heterogeneous distribution of the dye. Here, the low-fluorescent elongated regions are interpreted as the hydrophilic bricks embedded in a fluorescent hydrophobic mortar. The experimental observation using RBHE can thus be compared to the the model calculations in Fig. 3f, here using $K_{M/B} = 10^3$, where the sharp lines indicate high concentration of the probe in the mortar and basically empty bricks. Lastly in Fig. 3g we present the calculated relative permeability $\widehat{P}$ for membranes with varying distribution coefficients. The normalised permeability is relative to a reference membrane with uniform solubility $K_{M/B} = 1$.

Diffusing molecules with low $K_{M/B}$, will take the shortest route with the lowest resistance to the flux, meaning a straight through path with little to no lateral transport. For molecules with high $K_{M/B}$, on the other hand, the expected transport route is tortuous and through the mortar only. The maximum permeability is obtained for molecules with intermediate values of $K_{M/B}$, which indicate a balance between the high solubility in the comparably large bricks, and the low solubility of the volumetrically smaller yet unavoidable mortar. Here we note that either way the diffusing compound has to penetrate through several layers of continuous mortar in order to travel past the membrane as a whole.

In the following sections we will study the effects of altering the properties and dimensions of the mortar and the bricks in the composite membrane. For all these examples, we present the calculated profiles of the relative permeability as a function of the oil/water partition coefficient of the added compound, $K_{oil/water}$. This can be seen as a characteristic of a given compound, which may then distribute in different ways between bricks and mortar ($K_{M/B}$) depending on the properties of the composite structure. In other words, by showing $K_{oil/water}$ instead of $K_{M/B}$, we can make direct comparisons of how the permeability of a compound with known $K_{oil/water}$ changes when the brick and mortar structure is altered. Note however the relationship $K_{oil/water} \cdot \Phi_{fluid} = K_{M/B}$.

3.2. Phase transition in the mortar lipids

The phase behavior of the stratum corneum mortar lipids can be altered by changes in the skin surroundings. An increase in the fraction of fluid lipids can be caused by, for example, increasing the hydration at the skin surface (commonly referred to as occlusion[24]) or addition of a penetration enhancer[22,25]. In Fig. 4 we present the relative permeability as a function of the partition coefficient $K_{oil/water}$. Here we illustrate the extreme case of melting all the lipids (red curve), and compared to the case when only 10% of the lipids are fluid (black curve). With a higher fraction of fluid lipids we get an increase in both the solubility and the effective diffusion coefficient in the lipid regions, as $S_M = S_{lipids} = S_{oil} \cdot \Phi_{fluid}$ and $D_M = D_{lipids} \approx D_{oil} \cdot \Phi_{fluid}$.

By melting the lipids from 10% to 100% we note that the (red) permeability curve is shifted by a factor of ten to the left, and a factor of ten upwards. This total shift is an effect from increasing the diffusion coefficient and the solubility at the same time. Their separate individual contributions gives rise to different shifts and these are discussed in the SI, see Sec. S1. The relationships between solubility, diffusion, and relative permeability makes it possible to make predictions for any S_M, D_M, and Φ_{fluid} or combination based solely on one single master curve as described in Eq. 16 where X described the change of the indexed entity.

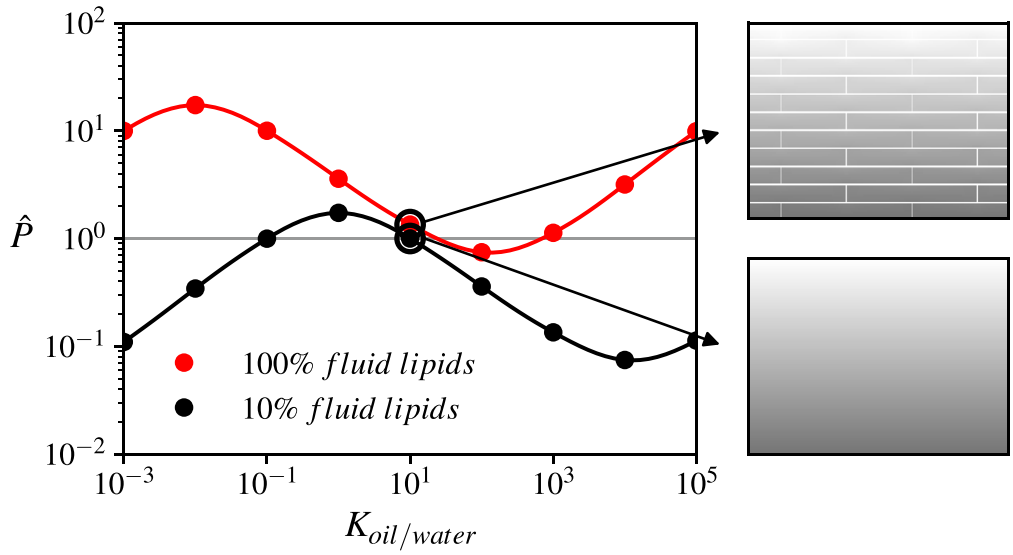

Fig. 4. Model calculations of the relative permeability $\hat{P}$ as a function of the oil/water partition coefficient when increasing the amount of fluid regions in the lipids. The black curve is the same as in Fig. 3g and compared to that red has ten times higher Φ_{fluid} which leads to an increase in both S_{lipids} and D_{lipids}.

$$\hat{P}(K_{M/B}, S_M, D_M) = \frac{\hat{P}\left(X_\Phi^{-1} X_D^{-1} \cdot K_{M/B}, X_S \cdot S_M, X_D \cdot D_M\right)}{\sqrt{X_S X_D}} \tag{16}$$

Finally, we note that the curve in Fig. 4 has both a local maximum and a local minimum. When $K_{oil/water}$ of the diffusing substances increases, the permeability of the compound through the corneocytes decreases, meaning that the lipid route is more favoured, and thus the tortuosity increases. After the local maximum, the effective permeability decreases until one reaches the maximum value of tortuosity. For higher $K_{oil/water}$ values, the partitioning towards the lipid domains is still increasing, whereas the tortuosity do not, and thus the relative permeability increases again.

3.3. Gradient in the properties of the mortar lipids

For all calculated results shown so far, we have assumed that the mortar lipids have the same properties at all depths inside the membrane. In most of the relevant situations, there are several gradients across the skin, which may also lead to changes in mortar lipid phase behavior at different positions within the skin membrane [3]. In Fig. 5 we illustrate how the relative membrane permeability is affected by introducing a gradient in the properties of the mortar lipids. We investigate two different scenarios. In the first example, we study the effect of increasing the fraction of fluid lipids in the upper layer of the SC (red curve), which may relate to the situations of occlusion or addition of a penetration enhancer [22,25]. Next, we instead reduce the fraction of fluid lipids in the upper part of SC as compared the the rest of the membrane (blue curve), which can be related to situations where the skin is exposed to dry conditions [26]. The changes in the amount of fluid lipids will directly impact both the effective diffusion coefficient and the effective solubility of the added compound in the mortar. An increase in the amount of the fluid lipids in the upper part of the membrane therefore leads to an increase in overall membrane permeability. Furthermore, the melting of lipids also causes a shift of the curve to slightly lower $K_{oil/water}$. The opposite happens if the fraction of fluid lipids is reduced in the upper layers of the mem-

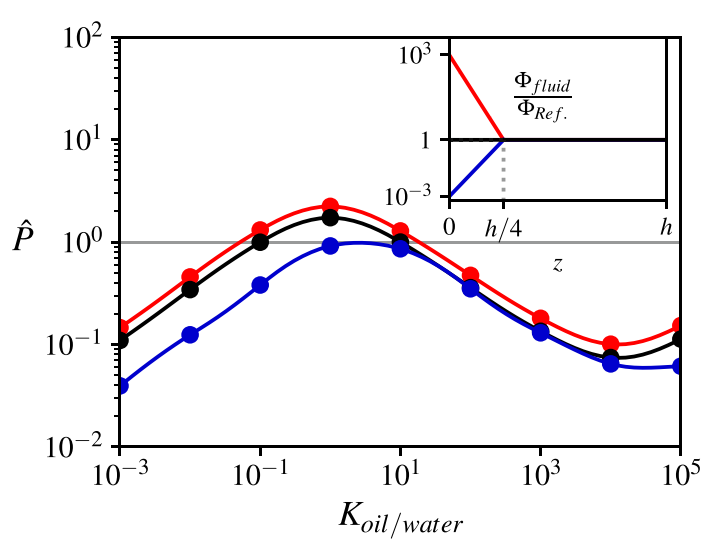

Fig. 5. Model calculations of the relative permeability $\hat{P}$ as a function of the oil/water partition coefficient for different profiles of the diffusion coefficients and solubilities (colors). The inset show the (normalized) fluid fraction in the lipids as a function of depth in the membrane z. Both lipid solubility and diffusion coefficient are proportional to Φ_{fluid}. Reference (black) is a system with zero gradients $D_{lipids}(z) = D_{lipids\ const.}$ and $S_{lipids}(z) = S_{lipids\ const.}$, and blue/red curve is lower/higher solubility of the probe close to the surface.

brane. Note that we in the example in Fig. 5 use a different reference system than for all other examples, with smaller fraction of fluid lipids $\Phi_{Ref.} = 10^{-3}$. This in order to better illustrate the effect of changing the lipid fluidity by using a steep gradient. For smaller gradients the trends are similar but the differences smaller.

3.4. Anisotropic mortar structure

In this section we explore how the membrane permeability is affected by an anisotropic mortar structure with different transport properties in the parallel and perpendicular directions, as expected for the multilamellar extracellular lipids [12]. In the calculated example in Fig. 6, the lateral component of the diffusion coefficient in the mortar $D_{lipids\|}$ is increased, while the vertical component $D_{lipids\perp}$ is that same as in all previous examples. For compounds that favor the path straight through the bricks above the tortuous pathway in the mortar (meaning low $K_{oil/water}$), the anisotropy in the mortar has no effect on the overall membrane permeability as there is little or no lateral diffusion. In the cases where the tortuous pathway is preferred (meaning high $K_{oil/water}$), there is a substantial effect on the membrane permeability by introducing anisotropy in the mortar.

3.5. Increasing Corneocyte Thickness

Next, we investigate the effect of changing the thickness of the corneocytes. This corresponds to the situation where the corneocytes take up water, for example in conditions of occluded (fully hydrated) skin [27]. In Fig. 7 we present the relative permeability for different corneocytes thicknesses t. We also include curves representing the exact analytic solutions (faded lines) in the limit of high or low $K_{oil/water}$. We start by noting that the analytic expressions are retrieved for both low and high $K_{oil/water}$ values. As expected, the calculations show that a thicker membrane gives a lower relative permeability, and vice verse. Yet, the maximum of the curves are all centered around the same value of $K_{oil/water}$. The

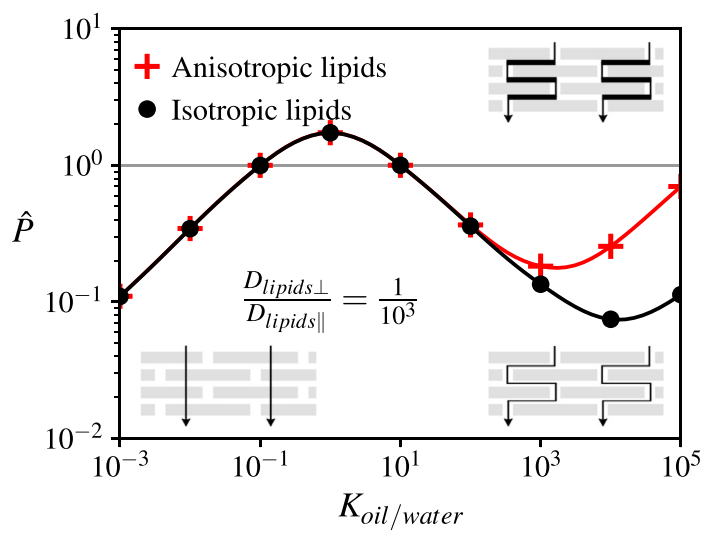

Fig. 6. Model calculations of the relative permeability $\widehat{P}$ as a function of the oil/water partition coefficient for a membrane with anisotropic (red) and isotropic (black) lipid properties. In the example calculations, the lateral component of the diffusion coefficient $D_{lipids\|}$ in the lipids is a thousand times larger than the vertical component $D_{lipids\perp} = 1$.

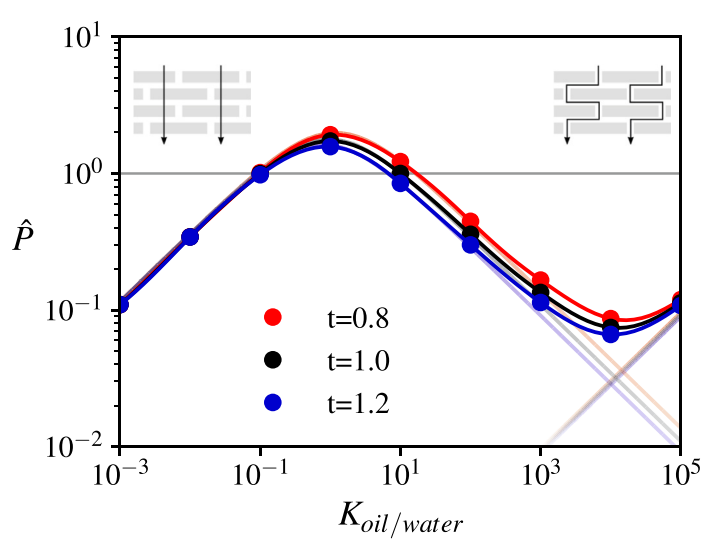

Fig. 7. Model calculations of the relative permeability $\widehat{P}$ as a function of the oil/water partition coefficient for different corneocytes thicknesses (colors). Faded lines corresponds to the analytic extreme cases using either very low or very high $K_{oil/water}$ described in Section 1.3.

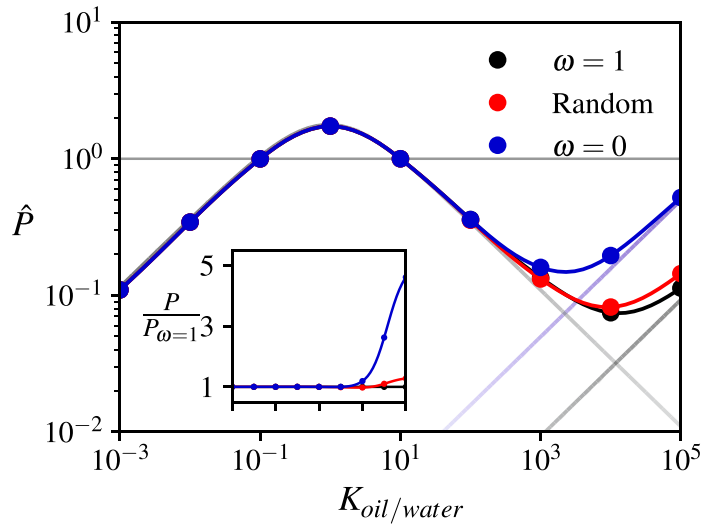

Fig. 8. Model calculations of the relative permeability $\widehat{P}$ as a function of the oil/water partition coefficient using different brick ordering (colors). The *x*-axis of the inset is identical to that of the outer figure. Here $\omega = 1$ gives brick positions as in Fig. 1a. The disordered systems uses a uniform random lateral displacement of each brick layer (see e.g. Fig. 2c). The $\omega = 0$ system can be described by bricks stacked perfectly on top of each other, giving a straight through path in the mortar. Each point of the 'Random' curve is a mean of three different random geometries which gives a standard deviation smaller than the size of the symbols. The inset show the relative permeability in reference to an $\omega = 1$ system. Faded lines corresponds to the analytic extreme cases using either very low or high $K_{oil/water}$ described in Section 1.3.

general finding is that that for the extreme cases of $K_{oil/water}$ (i.e. very low or high), the permeability is basically unaffected by the changes in brick thickness, and it is only for intermediate values of $K_{oil/water}$ that we observe a clear effect on the membrane permeability.

3.6. Lateral arrangement of Corneocytes

In Fig. 8 we present how the relative permeability depends on the lateral arrangements of the corneocytes, as defined by the offset parameters $\omega = l_{\rightarrow}/l_{\leftarrow}$ (see Fig. 2c). The results are based on three different offset ratios; $\omega = 1$ which gives a maximal tortuous path for any compound that exclusively pass through the the lipid mortar, $\omega = 0$ which gives the shortest path through the mortar (straight through membrane), and random lateral displacement of the corneocytes (see for example brick and mortar system in Fig. 2c). First, we note that the maximal tortuous path $\omega = 1$ (red curve) and random lateral displacement of the corneocytes (black curve) are strikingly similar. There are small differences at high $K_{oil/water}$ but for other values the calculated curves are all but indistinguishable from one another. Therefore, the highly symmetric model using $\omega = 1$ seems to capture the key features of models using random arrangement of bricks, which likely also the most relevant scenario for most biological membrane systems and technical applications. On the other hand, when the bricks are perfectly stacked on top of each other ($\omega = 0$) there is a substantial difference in permeability in contrast to the other more tortuous paths at high $K_{oil/water}$. For $\omega = 0$ there is a straight path in the mortar through the membrane and thus diffusing hydrophobic compounds can travel the shortest possible path in the lipid mortar without encountering any hydrophilic corneocyte bricks. For other values of ω the compound has to zigzag through the structure and thus take a longer path.

4. Conclusions

We have presented a model accounting for steady-state diffusion through different routes in any heterogeneous membranes which gives concentration profiles, permeabilities and fluxes. The approach relies on a formulation of generalized Fick's first law for steady-state diffusion which in a simple way accounts for activity coefficient, diffusion coefficient, and solubility all at once. Based on the presented theoretical foundation we then utilize Mesh analysis to build a framework that account for the diffusion through different pathways in composite membranes, taking into account the solubility of the diffusing molecules in the different regions. The output from this model show good agreement with experimental data on the distribution of different fluorescent probes inside stratum corneum. Furthermore, the numerical calculations agree with available exact analytic expressions for brick and mortar models for the extreme cases where the bricks either are completely impermeable or when they do not provide any resistance to the flux.

By using the presented model we studied the effects of changing the internal structure in the brick and mortar model, including anisotropic mortar structure mimicking a lamellar lipid arrangement, increased thickness of the bricks mimicking corneocyte swelling, and finally lateral arrangement of the bricks inside the brick and mortar membrane. For hydrophilic diffusing substances, none of these changes shown any notable effect on the overall permeability, while both the anisotropic mortar structure and the lateral arrangement of the brick strongly impact the permeability of the most hydrophobic compounds.

Declaration of Competing Interest

The authors declare that they have no known competing financial interests or personal relationships that could have appeared to influence the work reported in this paper.

Acknowledgements

We want to acknowledge the Swedish Research Council (ES, Grant No. 2019–05296) and L'Oréal for funding. The Centre for Cellular Imaging at the University of Gothenburg and the National Microscopy Infrastructure, NMI (No. VR-RFI 2016–00968), are acknowledged for providing access to laser scanning microscopy and kind support from the staff.

Appendix A. Supplementary material

Supplementary data associated with this article can be found, in the online version, at https://doi.org/10.1016/j.jcis.2022.11.013.

References

[1] A.S. Michaels, S.K. Chandrasekaran, J.E. Shaw, Drug permeation through human skin: Theory andinvitro experimental measurement, AIChE Journal 21 (5) (1975) 985–996, https://doi.org/10.1002/aic.690210522.

[2] I. Iwai, H. Han, L. den Hollander, S. Svensson, L.-G. Öfverstedt, J. Anwar, J. Brewer, M. Bloksgaard, A. Laloeuf, D. Nosek, S. Masich, L.A. Bagatolli, U. Skoglund, L. Norlén, The human skin barrier is organized as stacked bilayers of fully extended ceramides with cholesterol molecules associated with the ceramide sphingoid moiety, Journal of Investigative Dermatology 132 (9) (2012) 2215–2225, https://doi.org/10.1038/jid.2012.43.

[3] E. Sparr, H. Wennerström, Responding phospholipid membranes–interplay between hydration and permeability, Biophysical Journal 81 (2) (2001) 1014–1028, https://doi.org/10.1016/s0006-3495(01)75759-1.

[4] K. Roger, M. Liebi, J. Heimdal, Q.D. Pham, E. Sparr, Controlling water evaporation through self-assembly, Proceedings of the National Academy of Sciences 113 (37) (2016) 10275–10280. doi:10.1073/pnas.1604134113. URL: doi: 10.1073/pnas.1604134113.

[5] E. Sparr, H. Wennerström, Diffusion through a responding lamellar liquid crystal: a model of molecular transport across stratum corneum, Colloids and Surfaces B: Biointerfaces 19 (2) (2000) 103–116, https://doi.org/10.1016/s0927-7765(00)00136-3.

[6] T.-F. Wang, G.B. Kasting, J.M. Nitsche, A multiphase microscopic diffusion model for stratum corneum permeability. i. formulation, solution, and illustrative results for representative compounds, Journal of Pharmaceutical Sciences 95 (3) (2006) 620–648, https://doi.org/10.1002/jps.20509.

[7] F. Yu, G.B. Kasting, A geometrical model for diffusion of hydrophilic compounds in human stratum corneum, Mathematical Biosciences 300 (2018) 55–63, https://doi.org/10.1016/j.mbs.2018.03.010.

[8] B. Stenqvist, E. Sparr, Tortuosity in the brick and mortar model based on chemical conduction, Chemical Engineering Science 223 (2020) 115729, https://doi.org/10.1016/j.ces.2020.115729.

[9] T.-F. Wang, G.B. Kasting, J.M. Nitsche, A multiphase microscopic diffusion model for stratum corneum permeability. i. formulation, solution, and illustrative results for representative compounds, Journal of pharmaceutical sciences 95 (3) (2006) 620–648.

[10] D. Feuchter, M. Heisig, G. Wittum, A geometry model for the simulation of drug diffusion through the stratum corneum, Computing and Visualization in Science 9 (2) (2006) 117–130.

[11] B. Stenqvist, The tea is a lie (Oct. 2022). doi:10.5281/zenodo.7068086. URL: https://doi.org/10.5281/zenodo.7068086

[12] D.F. Evans, H. Wennerström, The colloidal domain: where physics, chemistry, biology, and technology meet., Advances in interfacial engineering series, Wiley-VCH, 1999.

[13] J.Z. Hearon, Some cellular diffusion problems based on onsager's generalization of fick's law, The Bulletin of Mathematical Biophysics 12 (2) (1950) 135–159, https://doi.org/10.1007/bf02478250.

[14] L. Onsager, S. Machlup, Fluctuations and irreversible processes, Physical Review 91 (6) (1953) 1505–1512, https://doi.org/10.1103/physrev.91.1505.

[15] I. Mills, T. Cvitaš, K. Homann, N. Kallay, Quantities, units and symbols in physical chemistry, Blackwell Scientific Publications, Oxford, 1993.

[16] J. Gottling, Node and mesh analysis by inspection, IEEE Transactions on Education 38 (4) (1995) 312–316, https://doi.org/10.1109/13.473148.

[17] E. Cussler, S.E. Hughes, W.J. Ward III, R. Aris, Barrier membranes, Journal of membrane science 38 (2) (1988) 161–174.

[18] M.E. Johnson, D. Blankschtein, R. Langer, Evaluation of solute permeation through the stratum corneum: Lateral bilayer diffusion as the primary transport mechanism, Journal of Pharmaceutical Sciences 86 (10) (1997) 1162–1172, https://doi.org/10.1021/js960198e.

[19] Guidance Document for the Conduct of Skin Absorption Studies, OECD, 2004. doi:10.1787/9789264078796-en. URL: https://doi.org/10.1787/9789264078796-en

[20] V. Kirejev, S. Guldbrand, J. Borglin, C. Simonsson, M. Ericson, Multiphoton microscopy. a powerful tool in skin research and topical drug delivery science, Journal of Drug Delivery Science and Technology 22 (3) (2012) 250–259, https://doi.org/10.1016/s1773-2247(12)50036-5.

[21] M.B. Ericson, C. Simonsson, S. Guldbrand, C. Ljungblad, J. Paoli, M. Smedh, Two-photon laser-scanning fluorescence microscopy applied for studies of human skin, Journal of Biophotonics 1 (4) (2008) 320–330, https://doi.org/10.1002/jbio.200810022.

[22] S. Björklund, A. Nowacka, J.A. Bouwstra, E. Sparr, D. Topgaard, Characterization of stratum corneum molecular dynamics by natural-abundance 13c solid-state NMR, PLoS ONE 8 (4) (2013) e61889, https://doi.org/10.1371/journal.pone.0061889.

[23] Q.D. Pham, G. Carlström, O. Lafon, E. Sparr, D. Topgaard, Quantification of the amount of mobile components in intact stratum corneum with natural-abundance 13c solid-state NMR, Physical Chemistry Chemical Physics 22 (12) (2020) 6572–6583, https://doi.org/10.1039/d0cp00079e.

[24] H. Zhai, H.I. Maibach, Effects of skin occlusion on percutaneous absorption: An overview, Skin Pharmacology and Physiology 14 (1) (2001) 1–10, https://doi.org/10.1159/000056328.

[25] Q.D. Pham, S. Björklund, J. Engblom, D. Topgaard, E. Sparr, Chemical penetration enhancers in stratum corneum – relation between molecular effects and barrier function, Journal of Controlled Release 232 (2016) 175–187, https://doi.org/10.1016/j.jconrel.2016.04.030.

[26] S. Björklund, J. Engblom, K. Thuresson, E. Sparr, A water gradient can be used to regulate drug transport across skin, Journal of Controlled Release 143 (2) (2010) 191–200, https://doi.org/10.1016/j.jconrel.2010.01.005.

[27] L. Norlén, A. Emilson, B. Forslind, Stratum corneum swelling. biophysical and computer assisted quantitative assessments, Archives of Dermatological Research 289 (9) (1997) 506–513, https://doi.org/10.1007/s004030050231.